

Modeling Ionic Polymer-Metal Composites with Space-Time Adaptive Multimesh *hp*-FEM

Deivid Pugal^{1,4}, Pavel Solin^{2,3,*}, Kwang J. Kim¹, and Alvo Aabloo⁴

¹ Mechanical Engineering Department, University of Nevada, Reno, NV, U.S.A.

² Department of Mathematics and Statistics, University of Nevada, Reno, NV, U.S.A.

³ Institute of Thermomechanics, Prague, Czech Republic

⁴ Institute of Technology, Tartu University, Estonia

Abstract. We are concerned with a model of ionic polymer-metal composite (IPMC) materials that consists of a coupled system of the Poisson and Nernst-Planck equations, discretized by means of the finite element method (FEM). We show that due to the transient character of the problem it is efficient to use adaptive algorithms that are capable of changing the mesh dynamically in time. We also show that due to large qualitative and quantitative differences between the two solution components, it is efficient to approximate them on different meshes using a novel adaptive multimesh *hp*-FEM. The study is accompanied with numerous computations and comparisons of the adaptive multimesh *hp*-FEM with several other adaptive FEM algorithms.

AMS subject classifications: 35Q84, 35Q05, 35J47

Key words: Ionic polymer-metal composites, IPMC, Nernst-Planck equation, Poisson equation, finite element method, FEM, adaptive multimesh *hp*-FEM

1 Introduction

Ionic Polymer-Metal Composites (IPMC) have been studied during the past two decades for their potential to serve as noiseless mechanoelectrical and electromechanical transducers [1, 4, 5, 7, 9, 10, 16]. The advantages of IPMC over other electroactive polymer actuators are low voltage bending, high strains ($> 1\%$), and an ability to work in wet environments. A typical IPMC consists of a thin sheet of polymer (often Nafion or Teflon) which is sandwiched between noble metal electrodes such as platinum or gold. When fabricated, the polymer membrane is saturated with certain solvent and ions such as water and H^+ . When a voltage is applied to the electrodes, the counter ions start migrating due to the imposed electric field. By dragging along the solvent, the osmotic pressure difference near the electrodes results in bending of the material (see Fig. 1).

*Corresponding author. Email addresses: david.pugal@gmail.com (D. Pugal), solin@unr.edu (P. Solin), kwangkim@unr.edu (K. Kim), alvo@ut.ee (A. Aabloo)

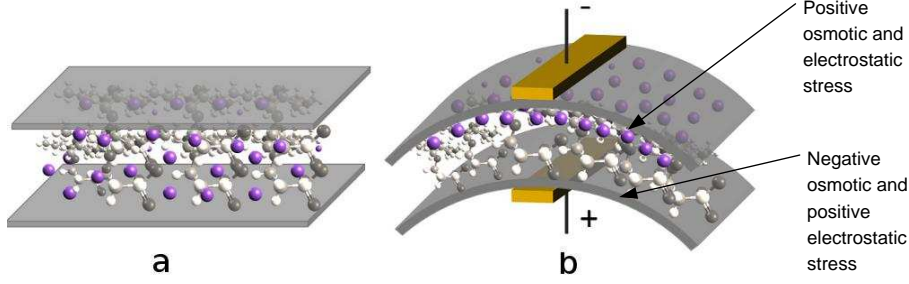


Figure 1: Conceptual model of the actuation of IPMC. Initial counter ion distribution (a) and the distribution and resulting bending after applying a voltage (b).

In this study we will model IPMC materials via a multiphysics coupled problem consisting of the Poisson and Nernst-Planck equations (abbreviated by PNP in the following). These equations are used to model charge transport in materials that include ionic migration, diffusion, and convection. The charge transport process is a key mechanism for electromechanical transduction.

The PNP system is highly nonlinear and for a typical domain with two electrodes, largest differences in charge concentration occur in a very narrow region near the boundary. The computing power required for a full scale problem is significant [8]. This is why we are interested in exploring adaptive algorithms – we hope to obtain meshes that are optimal in terms of calculation time and calculation error.

The Nernst-Planck equation for a mobile species — in our case for counter ions — has the form

$$\frac{\partial C}{\partial t} + \nabla \cdot (-D \nabla C - \mu F C \nabla \phi) = 0. \quad (1.1)$$

Here C stands for the counter ion concentration with the initial value of C_0 , D is diffusion, μ mobility, F Faraday constant, and ϕ voltage. We have neglected the velocity of the species as in our case it can be assumed zero. The Poisson equation has the form

$$-\nabla^2 \phi = \frac{F \rho}{\varepsilon} \quad (1.2)$$

where ε is the absolute dielectric permittivity. The charge density $\rho = C - C_0$ where C_0 is a constant anion concentration.

The outline of the paper is as follows: Section 2 shows that the solution components C and ϕ have very different behavior, which is the reason why it is difficult to find a common mesh that would be optimal for both of them. This explains why we are interested in approximation them on individual meshes equipped with mutually independent adaptivity mechanisms. The PNP model is presented in Section 3 where also its weak formulation for the Newton's method is derived. Section 4 presents a brief overview of a novel

adaptive multimesh hp -FEM method [3, 12–14] that is used to solve the problem numerically. Numerical results and comparisons are presented in Section 5, and conclusion and outlook are drawn in Section 6.

2 Motivation

In this section we use a simplified one-dimensional PNP model to illustrate the principal difficulties encountered in the numerical solution. Table 1 shows relevant constants.

Table 1: Constants used in the Poisson-Nernst-Planck system of equations.

Constant	Value	Unit	Description
D	10×10^{-11}	$\frac{m^2}{s}$	Diffusion constant
z	1	-	Charge number
F	96,485	$\frac{C}{mol}$	Faraday number
R	8.31	$\frac{J}{mol \cdot K}$	The gas constant
$\mu (= \frac{D}{RT})$	4.11×10^{-14}	$\frac{s}{mol \cdot K}$	Mobility
C_0	1,200	$\frac{mol}{m^3}$	Anion concentration
ε	0.025	$\frac{F}{m}$	Electric permittivity
l	200×10^{-6}	m	length scale

Fig. 2 shows a typical solution for C and ϕ at $t = 0.1$ s and $t = 3.0$ s.

The reader can observe that the solution has two notable characteristics: For the most part of the domain Ω , the gradient $\nabla C = 0$. Close to $\partial\Omega_2$, ∇C is nonzero and moving in time, and ∇C is very large at $\partial\Omega_1$. At the same time, ϕ is a “nice” smooth function for the most part of Ω but it has a large gradient at $\partial\Omega_2$. This makes the choice of an optimal mesh highly problematic. Even if the solution was stationary, an optimal mesh for C could never be optimal for ϕ and vice versa.

Furthermore, the shape of the solution in Fig. 2 suggests that the polynomial degree of finite elements in the middle of the domain Ω and near the boundaries $\partial\Omega_1$, $\partial\Omega_2$ should be different — large high-degree elements should be used in the middle of the domain while small low-degree ones should be used in the boundary layers. The qualitative differences in the solution components C and ϕ also suggest that using different meshes would be beneficial.

3 Model

We consider a rectangular 2D domain $\Omega \subset \mathbb{R}^2$ with boundaries $\partial\Omega_{1..4} \subset \partial\Omega$, shown in Fig. 3.

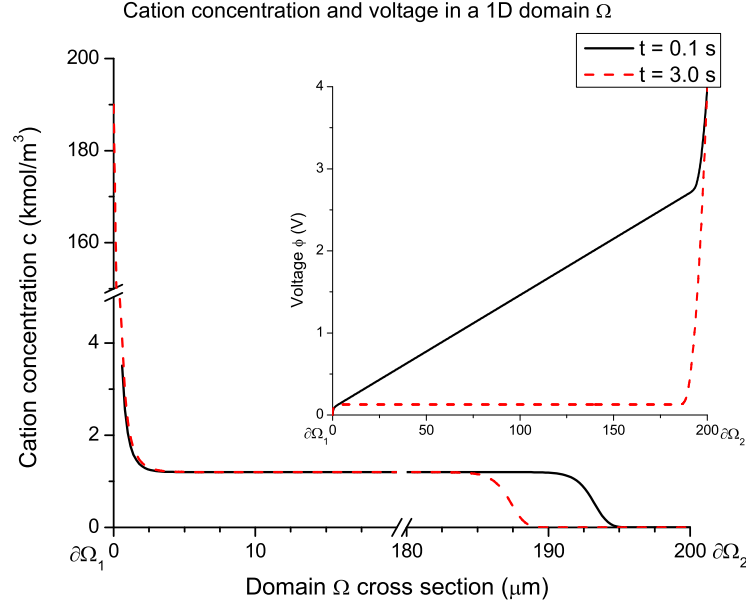


Figure 2: Sample concentration C and voltage ϕ in a 1D domain $\Omega \subset \mathbb{R}$. Dirichlet boundary conditions ($V_{\partial\Omega_1} = 0$ V and $V_{\partial\Omega_2} = 4$ V) were applied to the Poisson equation (1.2) and Neumann conditions to the Nernst-Planck equation (1.1).

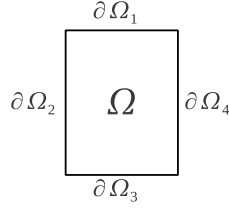


Figure 3: Calculation domain $\Omega \subset \mathbb{R}^2$ with boundaries $\partial\Omega_{1\dots 4} \subset \partial\Omega$.

As there is no flow through the domain's boundary, Eq. (1.1) is equipped with a Neumann boundary condition

$$-D \frac{\partial C}{\partial n} - \mu F C \frac{\partial \phi}{\partial n} = 0. \quad (3.1)$$

Furthermore, we prescribe a positive constant voltage V_{pos} on Ω_1 and zero voltage on Ω_3 :

$$\phi_{\partial\Omega_1} = V_{pos}, \quad (3.2)$$

$$\phi_{\partial\Omega_3} = 0. \quad (3.3)$$

On the rest of the boundary, ϕ has zero normal derivatives, and thus we prescribe a

Neumann boundary condition

$$\frac{\partial \phi_{\Omega_2}}{\partial n} = \frac{\partial \phi_{\Omega_4}}{\partial n} = 0. \quad (3.4)$$

3.1 Weak form of the PNP system

To make our results easily reproducible, in the following we present the derivation of weak forms of Eqs. (1.1) and (1.2), as well as formulas for the Jacobian matrix and residual vector that are used in actual computations. To simplify notation, we use dimensionless formulation of Eqs. (1.1) and (1.2). The following new notations for the independent variables x, y, t and for the dependent variables C and ϕ are used [2]:

$$X = \frac{x}{l}, \quad Y = \frac{y}{l}, \quad \tau = \frac{tD}{\lambda_D l}, \quad \varphi = \frac{\phi F}{RT}, \quad c = \frac{C}{C_0}. \quad (3.5)$$

Here λ_D is the Debye screening length and it is expressed as follows [2]:

$$\lambda_D = \sqrt{\frac{\epsilon RT}{2F^2 C_0}}. \quad (3.6)$$

After inserting variables (3.5) into Eq. (1.1) the Nernst-Planck equation and Poisson equation become:

$$\frac{DC_0}{\lambda_D l} \frac{\partial c}{\partial \tau} + \frac{1}{l} \nabla_d \cdot \left(-\frac{DC_0}{l} \nabla_d c - c \frac{DC_0}{l} \nabla_d \varphi \right) = 0 \quad (3.7)$$

$$-\frac{\epsilon RT}{l^2 F^2 C_0} \nabla_d^2 \varphi = c - 1, \quad (3.8)$$

where

$$\nabla_d = \left(\frac{\partial}{\partial X}, \frac{\partial}{\partial Y} \right). \quad (3.9)$$

After simplifying Eqs. (3.7) and (3.8) and denoting

$$\epsilon = \frac{\lambda_D}{l}, \quad (3.10)$$

the dimensionless form of the PNP system of equations is

$$\frac{\partial c}{\partial \tau} - \epsilon \nabla_d^2 c - \epsilon \nabla_d \cdot (c \nabla_d \varphi) = 0, \quad (3.11)$$

$$-\nabla_d^2 \varphi = \frac{c-1}{2\epsilon^2}. \quad (3.12)$$

Boundary condition Eq. (3.1) has the form

$$-\frac{\partial c}{\partial n} - c \frac{\partial \varphi}{\partial n} = 0. \quad (3.13)$$

As the second derivatives of both c and φ are present in the equations, the appropriate function space for them is the Sobolev space $V = H^1(\Omega)$ where

$$H^1(\Omega) = \left\{ v \in L^2(\Omega); \nabla_d v \in [L^2(\Omega)]^2 \right\}.$$

In order to derive the weak form of the Nernst-Planck equation Eq. (3.11), we first multiply it with a test function $v^c \in V$ and integrate over the domain Ω ,

$$\int_{\Omega} \frac{\partial c}{\partial \tau} v^c d\mathbf{x} - \int_{\Omega} \epsilon \nabla_d^2 c v^c d\mathbf{x} - \int_{\Omega} \epsilon \nabla_d c \cdot \nabla_d \varphi v^c d\mathbf{x} - \int_{\Omega} \epsilon c \nabla_d^2 \varphi v^c d\mathbf{x} = 0. \quad (3.14)$$

Applying the Green's first identity to the terms that contain second derivatives, we obtain

$$\begin{aligned} & \int_{\Omega} \frac{\partial c}{\partial \tau} v^c d\mathbf{x} + \epsilon \int_{\Omega} \nabla_d c \cdot \nabla_d v^c d\mathbf{x} - \epsilon \int_{\Omega} \nabla_d c \cdot \nabla_d \varphi v^c d\mathbf{x} \\ & + \epsilon \int_{\Omega} \nabla_d (c v^c) \cdot \nabla_d \varphi d\mathbf{x} - \epsilon \int_{\partial\Omega} \frac{\partial c}{\partial n} v^c d\mathbf{S} - \int_{\partial\Omega} \epsilon \frac{\partial \varphi}{\partial n} c v^c d\mathbf{S} = 0. \end{aligned} \quad (3.15)$$

Expanding the nonlinear term and using the boundary condition (3.13), we have

$$\begin{aligned} & \int_{\Omega} \frac{\partial c}{\partial \tau} v^c d\mathbf{x} + \epsilon \int_{\Omega} \nabla_d c \cdot \nabla_d v^c d\mathbf{x} - \epsilon \int_{\Omega} \nabla_d c \cdot \nabla_d \varphi v^c d\mathbf{x} \\ & + \epsilon \int_{\Omega} \nabla_d \varphi \cdot \nabla_d c v^c d\mathbf{x} + \epsilon \int_{\Omega} c (\nabla_d \varphi \cdot \nabla_d v^c) d\mathbf{x} = 0. \end{aligned} \quad (3.16)$$

After the third and fourth terms cancel out, we obtain the final weak form of the Nernst-Planck equation

$$\int_{\Omega} \frac{\partial c}{\partial \tau} v^c d\mathbf{x} + \epsilon \int_{\Omega} \nabla_d c \cdot \nabla_d v^c d\mathbf{x} + \epsilon \int_{\Omega} c (\nabla_d \varphi \cdot \nabla_d v^c) d\mathbf{x} = 0. \quad (3.17)$$

Analogously we derive also the weak form of the Poisson equation (3.12),

$$- \int_{\Omega} \nabla_d^2 \varphi v^{\varphi} d\mathbf{x} - \frac{1}{2\epsilon^2} \left[\int_{\Omega} c v^{\varphi} d\mathbf{x} - \int_{\Omega} v^{\varphi} d\mathbf{x} \right] = 0. \quad (3.18)$$

Performing integration by parts and taking into account the boundary conditions for φ , we obtain

$$\int_{\Omega} \nabla_d \varphi \cdot \nabla_d v^{\varphi} d\mathbf{x} - \frac{1}{2\epsilon^2} \left[\int_{\Omega} c v^{\varphi} d\mathbf{x} - \int_{\Omega} v^{\varphi} d\mathbf{x} \right] = 0. \quad (3.19)$$

3.2 Jacobian matrix and residual vector for the Newton's method

To employ the Newton's method for the nonlinear system (3.17), (3.19), formulas for the Jacobian matrix and residual vector need to be derived. Time discretization will be performed using the second-order Crank-Nicolson method. The unknown solution components c^{n+1} and φ^{n+1} at the end of the time step $\delta\tau$ are expressed as linear combinations of finite element basis functions v_k^c and v_k^φ with unknown coefficients,

$$c^{n+1} = c(Y^{n+1}) = \sum_{k=1}^{N^c} y_k^c v_k^c, \quad (3.20)$$

$$\varphi^{n+1} = \varphi(Y^{n+1}) = \sum_{k=1}^{N^\varphi} y_k^\varphi v_k^\varphi. \quad (3.21)$$

Here Y^{n+1} is a coefficient vector of length $N^c + N^\varphi$ comprising the unknown solution coefficients y_k^c and y_k^φ (in this order). We will also be using $c^n = c(Y^n)$ and $\varphi^n = \varphi(Y^n)$ for the previous time step solutions.

With the notation (3.20), (3.21), the time discretized Eq. (3.17) leads to the formula for the first part F^c of the residual vector F ,

$$\begin{aligned} F_i^c(Y) = & \int_{\Omega} \frac{c(Y)}{\delta\tau} v_i^c d\mathbf{x} - \int_{\Omega} \frac{c^n}{\delta\tau} v_i^c d\mathbf{x} \\ & + \frac{1}{2}\epsilon \left[\int_{\Omega} \nabla_d c(Y) \cdot \nabla_d v_i^c d\mathbf{x} + \int_{\Omega} \nabla_d c^n \cdot \nabla_d v_i^c d\mathbf{x} \right. \\ & \left. + \int_{\Omega} c(Y) (\nabla_d \varphi(Y) \cdot \nabla_d v_i^c) d\mathbf{x} + \int_{\Omega} c^n (\nabla_d \varphi^n \cdot \nabla_d v_i^c) d\mathbf{x} \right] \end{aligned} \quad (3.22)$$

where $i = 1, 2, \dots, N^c$. Analogously, Eq. (3.19) defines the second part F^φ of the residual vector F ,

$$F_i^\varphi(Y) = \int_{\Omega} \nabla_d \varphi(Y) \cdot \nabla_d v_i^\varphi d\mathbf{x} - \frac{1}{2\epsilon^2} \left[\int_{\Omega} c(Y) v_i^\varphi d\mathbf{x} - \int_{\Omega} v_i^\varphi d\mathbf{x} \right] \quad (3.23)$$

where $i = N^c + 1, N^c + 2, \dots, N^c + N^\varphi$. The nonlinear discrete problem that needs to be solved at the end of each time step thus has the form $F(Y) = 0$.

The Jacobian matrix $J(Y) = DF/DY$ has a 2×2 block structure,

$$J(Y) = \begin{pmatrix} \frac{\partial F_i^c}{\partial y_j^c} & \frac{\partial F_i^c}{\partial y_j^\varphi} \\ \frac{\partial F_i^\varphi}{\partial y_j^c} & \frac{\partial F_i^\varphi}{\partial y_j^\varphi} \end{pmatrix}, \quad (3.24)$$

and its entries are obtained by calculating the partial derivatives of F with respect to the components of the coefficient vector Y . For this it is useful to realize that

$$\frac{\partial c(Y)}{\partial y_j^c} = v_j^c, \quad \frac{\partial \nabla_d c(Y)}{\partial y_j^c} = \nabla_d v_j^c, \quad \text{etc..}$$

We obtain

$$\frac{\partial F_i^c}{\partial y_j^c}(Y) = \int_{\Omega} \frac{1}{\delta\tau} v_j^c v_i^c d\mathbf{x} + \frac{1}{2}\epsilon \left[\int_{\Omega} \nabla_d v_j^c \cdot \nabla_d v_i^c d\mathbf{x} + \int_{\Omega} v_j^c (\nabla_d \varphi(Y) \cdot \nabla_d v_i^c) d\mathbf{x} \right], \quad (3.25)$$

$$\frac{\partial F_i^c}{\partial y_j^{\varphi}}(Y) = \frac{1}{2}\epsilon \int_{\Omega} c(Y) \left(\nabla_d v_j^{\varphi} \cdot \nabla_d v_i^c \right) d\mathbf{x}, \quad (3.26)$$

$$\frac{\partial F_i^{\varphi}}{\partial y_j^c}(Y) = -\frac{1}{2\epsilon^2} \int_{\Omega} v_j^c v_i^{\varphi} d\mathbf{x}, \quad (3.27)$$

$$\frac{\partial F_i^{\varphi}}{\partial y_j^{\varphi}}(Y) = \int_{\Omega} \nabla_d v_j^{\varphi} \cdot \nabla_d v_i^{\varphi} d\mathbf{x}. \quad (3.28)$$

3.3 Newton's iteration

At the beginning of the $(n+1)$ st time step we set $Y_0^{n+1} = Y^n$, where Y^n is the coefficient vector that was calculated in the n th time step (or coming from the initial condition if $n=0$). We set $k=0$ and run the Newton's iteration

$$\begin{aligned} J(Y_k^{n+1}) \delta\tau Y_{k+1}^{n+1} &= -F(Y_k^{n+1}), \\ Y_{k+1}^{n+1} &= Y_k^{n+1} + \delta\tau Y_{k+1}^{n+1}, \\ k &:= k+1 \end{aligned}$$

over k until it converges. Then we set $Y^{n+1} := Y_k^{n+1}$. We use a combined stopping criterion that makes sure that both the norm of the residual vector $\|F(Y^{n+1})\|$ as well as the norm of the increment $\|\delta Y^{n+1}\|$ are sufficiently small.

4 Adaptive hp -FEM and the Open-Source Library Hermes

In traditional low-order FEM (based on piecewise-linear or piecewise quadratic elements), refining an element is not algorithmically complicated, and so the most difficult part is to find out what elements should be refined. To do this, various techniques ranging from rigorous guaranteed a-posteriori error estimates to heuristic criteria such as residual error indicators or error indicators based on steep gradients are employed.

However, none of these approaches is suitable for multiphysics coupled problems or higher-order finite element methods: Rigorous guaranteed error estimates only exist for very simple problems (such as linear elliptic PDE) and only for low-order finite elements. Heuristic techniques are usually somehow doable for all problems, but they fail in more complicated situations. Moreover, they lack a transparent relation to the true approximation error and thus they may give wrong results.

Automatic adaptivity in higher-order finite element methods (hp -FEM) is much different from adaptivity in low-order FEM. Firstly, analytical error estimates capable of

guiding adaptive hp -FEM do not exist even for the simplest linear elliptic equations, not speaking about nonlinear multiphysics coupled systems. Secondly, a higher-order element can be refined in many different ways, as illustrated in Fig. 4.

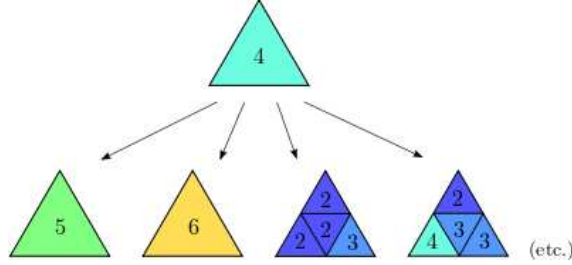


Figure 4: Many possible refinement candidates for a fourth-order element.

The number of possible element refinements is implementation dependent. In general it is very low in h -adaptivity and p -adaptivity, and much higher in hp -adaptivity. Moreover, this number grows very fast when anisotropic refinements are enabled.

4.1 The Hermes Library

Hermes[†] is a free and open-source C++ library that implements higher-order finite elements approximations and adaptive hp -FEM. It supports 8 different adaptivity modes – three isotropic and five anisotropic. The isotropic refinements are h -isotropic (H_ISO), p -isotropic (P_ISO), hp -isotropic (HP_ISO). Anisotropic refinement modes are h -anisotropic (H_ANISO), hp -anisotropic- h (HP_ANISO_H), p -anisotropic (P_ANISO), hp -anisotropic- p (HP_ANISO_P), and hp -anisotropic (HP_ANISO). The eight adaptivity modes are summarized in Fig. 5. It must be noted that in case of HP_ANISO_H, only element size is adapted anisotropically whereas polynomial degree is adapted isotropically. The opposite holds true for HP_ANISO_P.

Note that triangular elements do not support anisotropic refinements. Due to the large number of refinement options, classical error estimators that provide a constant error estimate per element, cannot be used to guide automatic hp -adaptivity. For this, one needs to know the shape of the approximation error. Hermes uses a pair of approximations with different orders of accuracy to obtain this information: coarse mesh solution and fine mesh solution [11]. The initial coarse mesh is read from the mesh file, and the initial fine mesh is created through its global refinement both in h and p . The fine mesh solution is the approximation of interest both during the adaptive process and at the end of computation. Global orthogonal projection of the fine mesh solution on the coarse mesh is used to extract the low-order part from the reference solution. The adaptivity algorithm is guided by the difference between the reference solution and its low-order part.

[†]<http://hpfem.org/hermes>

<i>CAND_LIST</i>	<i>H-candidates</i>	<i>ANISO-candidates</i>		<i>P-candidates</i>
H_ISO	<div> <div>h</div> <div>v</div> <div>h</div> <div>v</div> </div>			<div>h</div> <div>v</div>
H_ANISO	<div> <div>h</div> <div>v</div> <div>h</div> <div>v</div> </div>	<div>h</div> <div>v</div>	<div>h</div> <div>v</div>	<div>h</div> <div>v</div>
P_ISO				<div>$h+\delta_0$</div> <div>$v+\delta_0$</div>
P_ANISO				<div>$h+\alpha_0$</div> <div>$v+\beta_0$</div>
HP_ISO	<div> <div>$\frac{1}{2}h+\delta_3$</div> <div>$\frac{1}{2}v+\delta_3$</div> <div>$\frac{1}{2}h+\delta_0$</div> <div>$\frac{1}{2}v+\delta_0$</div> </div>			<div>$h+\delta_0$</div> <div>$v+\delta_0$</div>
HP_ANISO_H	<div> <div>$\frac{1}{2}h+\delta_3$</div> <div>$\frac{1}{2}v+\delta_3$</div> <div>$\frac{1}{2}h+\delta_0$</div> <div>$\frac{1}{2}v+\delta_0$</div> </div>	<div>$h+\delta_1$</div> <div>$\frac{1}{2}v+\delta_1$</div>	<div>$\frac{1}{2}h+\delta_0$</div> <div>$\frac{1}{2}h+\delta_1$</div>	<div>$h+\delta_0$</div> <div>$v+\delta_0$</div>
HP_ANISO_P	<div> <div>$\frac{1}{2}h+\alpha_3$</div> <div>$\frac{1}{2}v+\beta_3$</div> <div>$\frac{1}{2}h+\alpha_0$</div> <div>$\frac{1}{2}v+\beta_0$</div> </div>			<div>$h+\alpha_0$</div> <div>$v+\beta_0$</div>
HP_ANISO	<div> <div>$\frac{1}{2}h+\alpha_3$</div> <div>$\frac{1}{2}v+\beta_3$</div> <div>$\frac{1}{2}h+\alpha_0$</div> <div>$\frac{1}{2}v+\beta_0$</div> </div>	<div>$h+\alpha_1$</div> <div>$\frac{1}{2}v+\beta_1$</div>	<div>$\frac{1}{2}h+\alpha_0$</div> <div>$\frac{1}{2}h+\alpha_1$</div>	<div>$h+\alpha_0$</div> <div>$v+\beta_0$</div>

Figure 5: Refinement candidates for every refinement mode for quad type elements.

Note that this approach to automatic adaptivity is PDE-independent and thus naturally applicable to a large variety of multiphysics coupled problems.

4.2 Multimesh *hp*-FEM

In multiphysics PDE systems such as Poisson-Nernst-Planck it can happen that one physical field is very smooth where others are not, as we illustrated in Fig. 2. If all the fields are approximated on the same mesh, then unnecessary refinements will be present in

smooth areas where they are not necessary. This can be very wasteful.

Hermes implements a novel adaptive multimesh *hp*-FEM [3, 12, 14] that makes it possible to approximate different fields on individual meshes, without breaking the monolithic structure of the coupling mechanism. For practical reasons, the meshes in the system are not allowed to be completely independent – they have a common coarse mesh that we call *master mesh*. The master mesh is there for algorithmic purposes only and it may not even be used for discretization purposes. Every mesh in the system is obtained from the master mesh via an arbitrary sequence of elementary refinements. Assembling is done on a *union mesh*, a geometrical union of all meshes in the system (imagine printing all meshes on transparencies and positioning them on top of each other).

The union mesh is not constructed physically in the computer memory – it merely serves as a hint to correctly transform the integration points while integrating over sub-elements of elements in the existing meshes. As a result, the multimesh discretization of the PDE system is monolithic in the sense that no physics is lost — all integrals in the discrete weak formulations are evaluated exactly up to the error in the numerical quadrature. The exact preservation of the coupling structure of multiphysics coupled problems makes the multimesh *hp*-FEM very different from various interpolation and projection based methods that suffer from errors made while transferring data between different meshes in the system.

5 Numerical Results and Comparisons

The solutions to the PNP problem exhibit a specific behavior that was described above. In order to find the best adaptive method to deal with this type of problems, we performed numerous computations using all adaptivity modes in both the single-mesh and multi-mesh regimes. In the numerical experiments we paid attention to the relative error, cumulative CPU time, and problem size in terms of number of degrees of freedom (DOF) in each time step. The scaled variables c and φ and the unscaled time t are used to present the solutions. The simulations were performed with physical time step of 0.05 s and the final time of 3.0 s was chosen as it is close to the time scaling constant τ .

We used two types of initial meshes — a finer mesh shown in Fig. 6 (b) was used for *p*-adaptivity and a very coarse initial mesh shown in Fig. 6 (a) was used for *h*-adaptivity and *hp*-adaptivity.

An example of the solution at $t = 0.1$ s and $t = 3.0$ s calculated with the HP_ANISO refinement mode is shown in Figs. 7 and 8.

The reader can see that at $t = 0.1$ s some ionic migration has already taken place and large concentration gradients near the boundaries $\partial\Omega_1$ and $\partial\Omega_3$ have formed. The figures also show that the meshes at $t = 0.1$ s and $t = 3.0$ s are different.

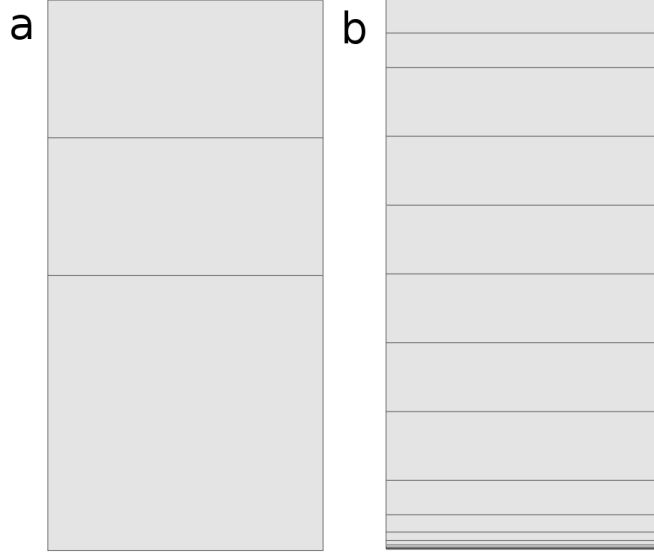


Figure 6: Initial coarse mesh (a) and refined mesh (b). The coarse mesh (a) and refined mesh (b) were used in the initial calculations, the latter one in case of p -adaptivity (including HP_ANISO_P).

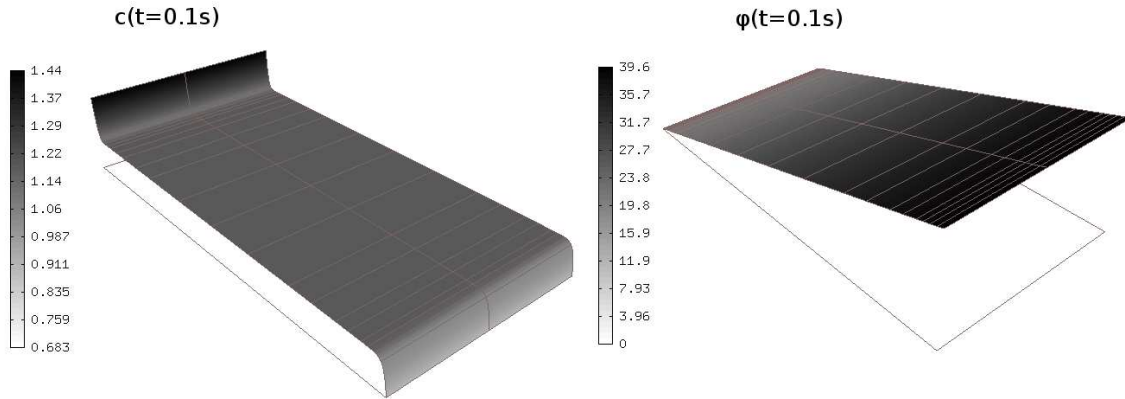


Figure 7: Scaled concentration c and voltage ϕ at $t=0.1$ s.

5.1 Comparison of single mesh low-order FEM and hp -FEM

First of all, the low-order FEM and hp -FEM were compared. A single mesh H_ANISO with polynomial degrees $p=1$ and $p=2$ were compared to HP_ANISO mode. The coarse initial mesh as shown in Fig. 6 (a) was used in the solutions. The results are shown in Figs. 9 and 10.

It can be seen that hp -FEM results in a shorter computing time and smaller number of DOF than the low-order FEM. The same holds true for H_ISO and HP_ISO modes. In fact, in case of H_ISO the relative error did not converge to the pre-set threshold value

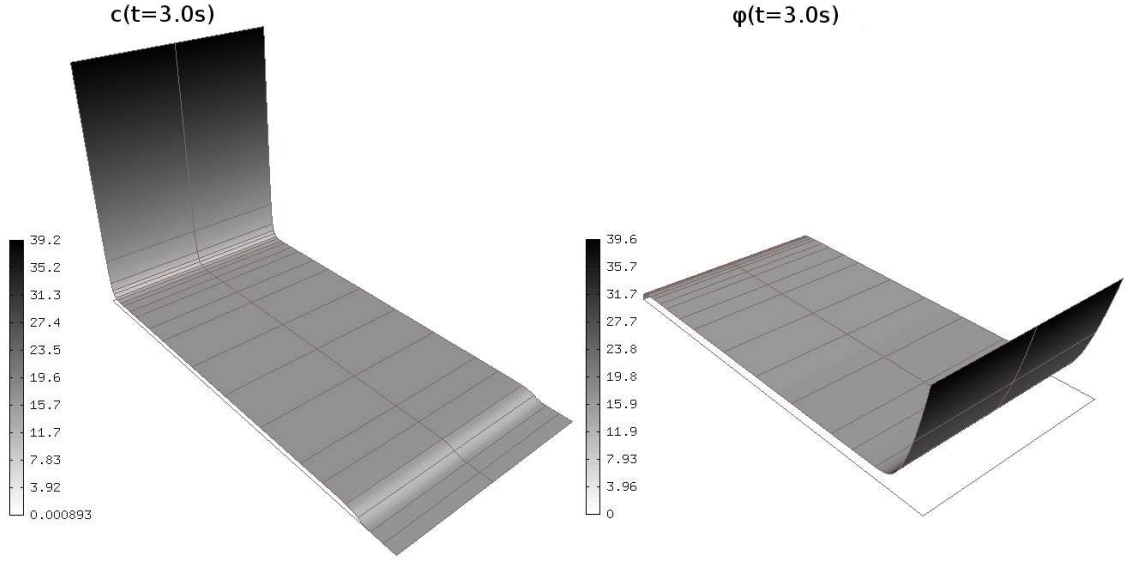


Figure 8: Scaled concentration c and voltage φ at $t=3.0$ s.

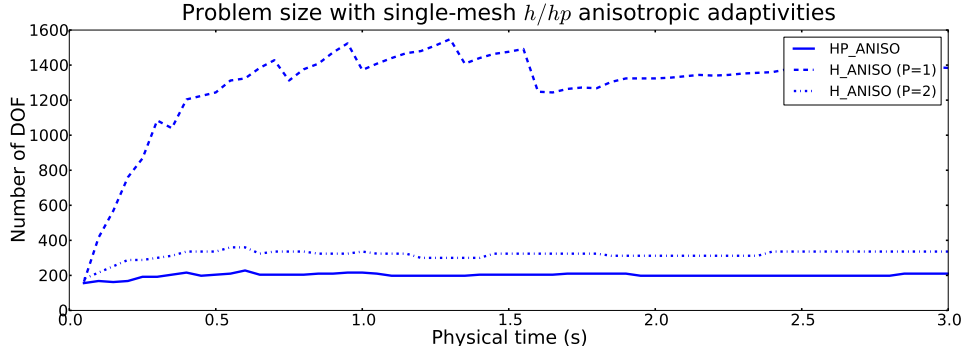


Figure 9: Number of degrees of freedom (DOF) as a function of physical time for single-mesh H_ANISO (in case of $p=1$ and $p=2$) and single-mesh HP_ANISO.

of 0.5% within acceptable range of degrees of freedom of $nDOF_{threshold} = 5000$. Therefore, the h -FEM solutions will be omitted from the further comparisons. Instead, only hp -FEM solutions on the coarse mesh and p -FEM solutions on the fine mesh will be discussed.

5.2 Comparison of single-mesh and multi-mesh hp -FEM

Running the simulation with different adaptivity modes and meshes showed that the multi-mesh hp -FEM configuration resulted in the smallest problems and similar error convergence compared to any single-mesh configuration. However, multi-mesh problems generally resulted in longer computing times. This is a known shortcoming of Hermes at this point and it is due to the fact that multi-mesh uses the union mesh (see

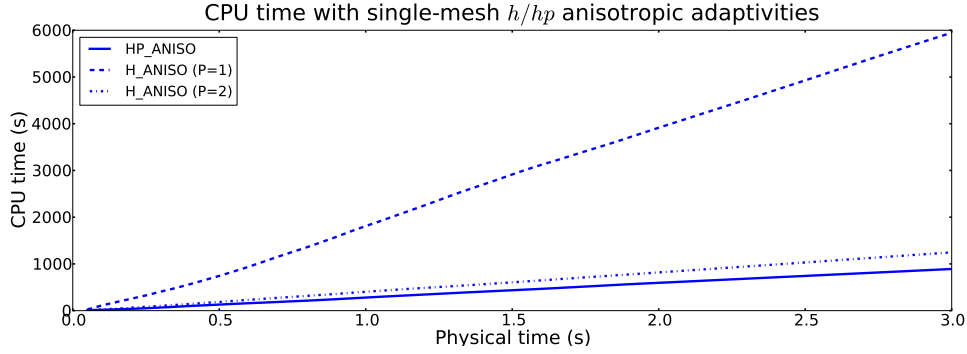


Figure 10: Cumulative CPU time as a function of physical time for single-mesh H_ANISO (in case of $p=1$ and $p=2$) and single mesh HP_ANISO.

Section 4) where the numerical integration of high order is done on very small elements. The problem size and computing time are illustrated for HP_ANISO adaptivity mode in Fig. 11 and Fig. 12. The same holds true for HP_ISO mode. It must be also noted that the error converged to or below 0.5% for all p -FEM and anisotropic hp -FEM results.

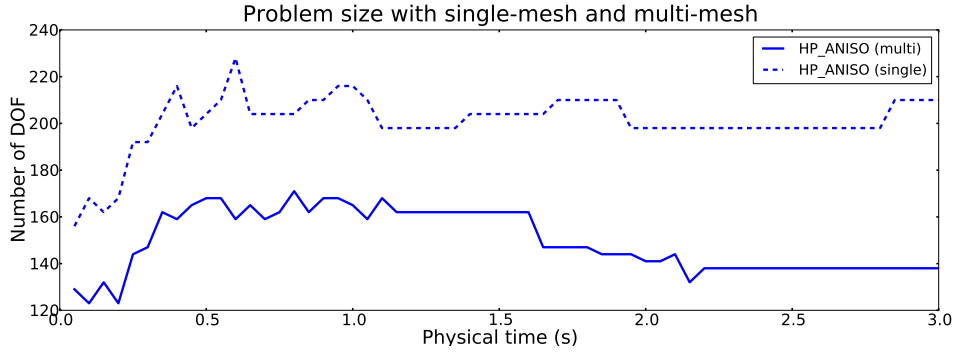


Figure 11: Number of DOF as a function of physical time for single-mesh and multi-mesh configurations with HP_ANISO adaptivity mode.

Figs. 13 and 14 show higher-order meshes in the adaptive multi-mesh hp -FEM computation for c and φ at $t=0.1$ s and $t=3.0$ s, respectively. Different colors mean different polynomial degrees. A diagonal pattern inside an element tells that the element has different polynomial degrees in the horizontal and vertical directions.

The result are in good agreement with Fig. 8 — in the vicinity of the boundaries $\partial\Omega_1$ and $\partial\Omega_3$, the concentration gradient is much greater than the voltage gradient. Therefore at $t=0.1$ s, the multi-mesh hp -FEM adaptivity algorithm has increased the maximum polynomial degree for the c -space to 6 while the maximum polynomial degree for the φ -space is 4. The meshes are not that different in the beginning of the calculation. However, one can also see that the mesh refinement for c at $t=3.0$ s is notably different compared to φ . For instance, the highest polynomial degree for c -space is 8 whereas for φ -space

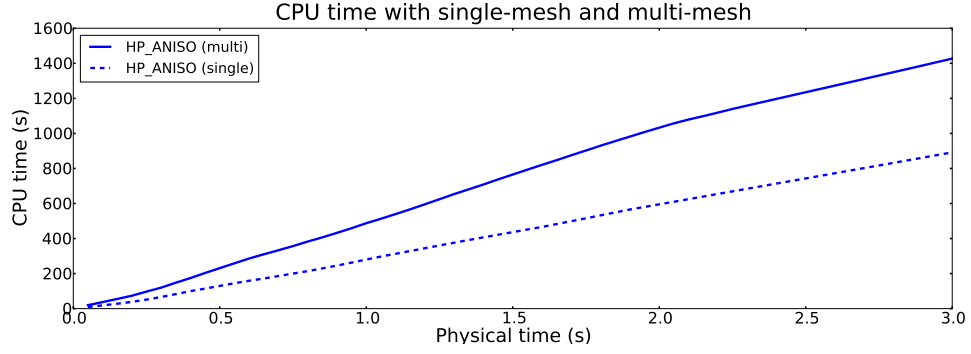


Figure 12: Cumulative CPU time as a function of physical time for single-mesh and multi-mesh configurations with HP_ANISO adaptivity mode.

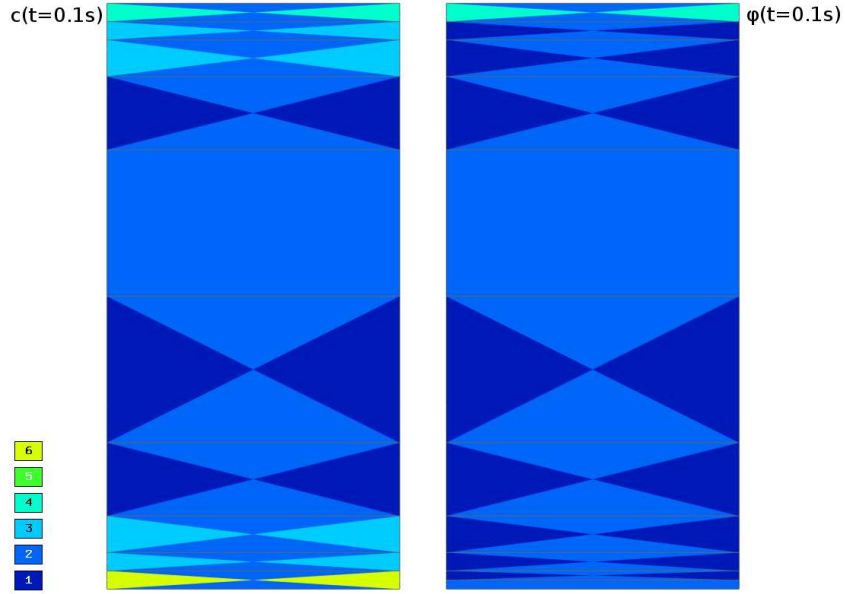


Figure 13: Higher-order FEM mesh for c and φ at $t=0.1$ s.

is 4. Since these results are representative for all adaptivity modes, only multi-mesh configurations are considered in the following.

5.3 Comparison of isotropic and anisotropic refinements

Next we would like to illustrate the role of anisotropic mesh refinements. Figs. 15 and 16 show typical results for the HP_ISO, HP_ANISO_H, HP_ANISO adaptivity modes in terms of DOF and cumulative CPU time. Fig. 17 shows corresponding error convergence. It can be seen that HP_ISO is notoriously inefficient as the error does not converge within the limited number of degrees of freedom of $nDOF_{threshold} = 5000$ and computing time is

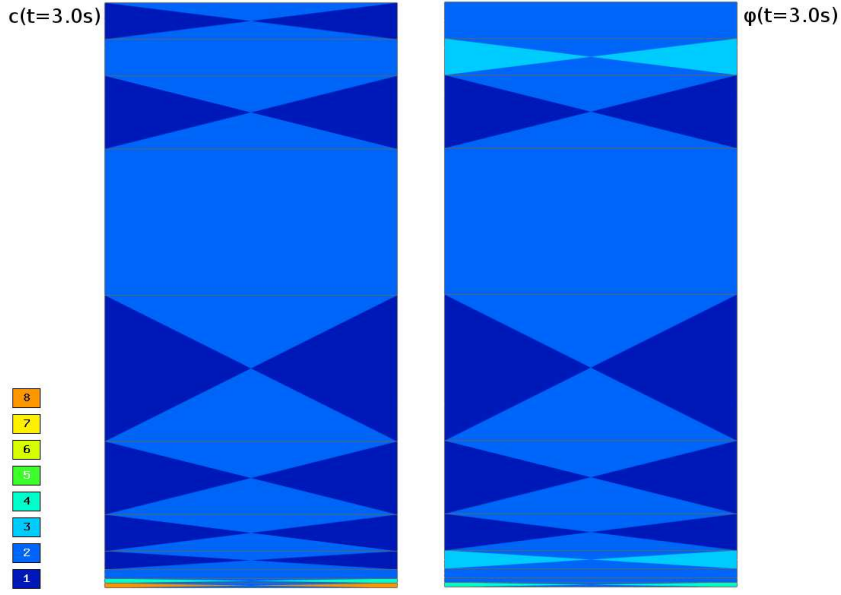


Figure 14: Higher-order FEM mesh for c and φ at $t=3.0$ s.

very large. Due to that fact, the calculation of HP_ISO was canceled before $t=3.0$ s.

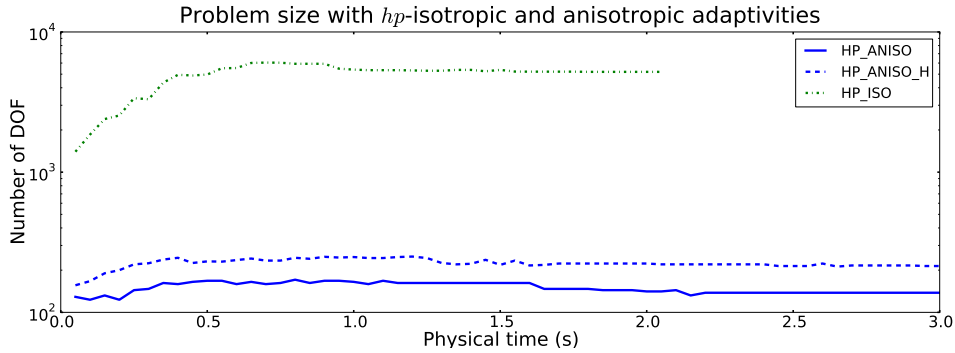


Figure 15: Number of DOF as a function of physical time for multi-mesh configurations with HP_ANISO, HP_ANISO_H, and HP_ISO adaptivity modes (log y scale).

Figs. 18 and 19 present a similar comparison for the P_ISO, P_ANISO, and HP_ANISO_P modes. Recall that these computations use a different initial mesh that was a-priori refined in space.

As a conclusion, the reader can see that the anisotropic adaptivity modes always perform better than the isotropic ones. In particular, HP_ANISO results into the smallest problem size. In the p -adaptivity group, HP_ANISO_P and P_ANISO lead to a small problem size consistently in each time step, whereas P_ISO yields large problems during the first time steps.

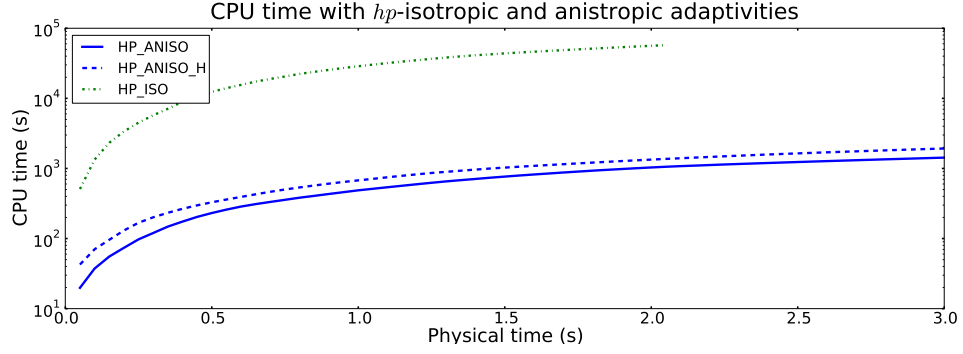


Figure 16: Cumulative CPU time as a function of physical time for multi-mesh configurations with HP_ANISO, HP_ANISO_H, and HP_ISO adaptivity modes (log y scale).

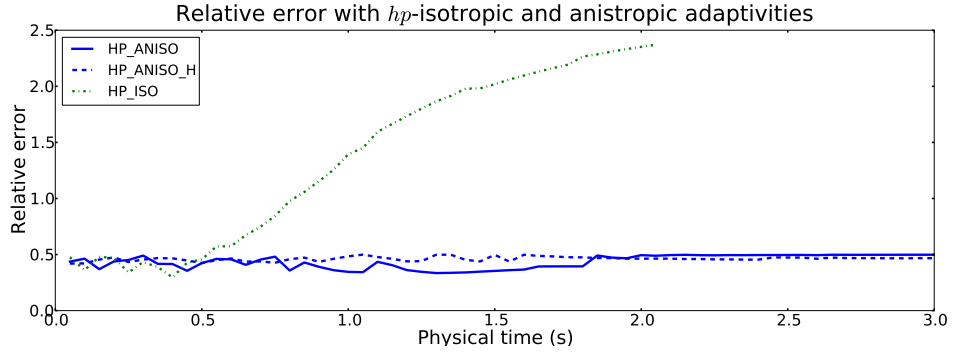


Figure 17: Relative solution error as a function of physical time for multi-mesh configurations with HP_ANISO, HP_ANISO_H, and HP_ISO adaptivity modes.

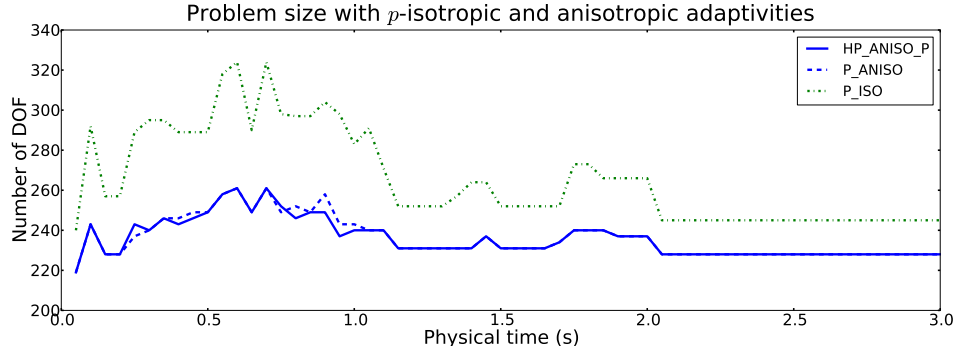


Figure 18: Number of DOF as a function of physical time for multi-mesh configurations with P_ISO, P_ANISO, and HP_ANISO_P adaptivity modes.

HP_ANISO also results in the fastest computing time among hp -adaptivity group whereas HP_ANISO_P results in the fastest overall computing time. This is due to the fact that HP_ANISO_P calculation is performed on the refined mesh. Regardless, the

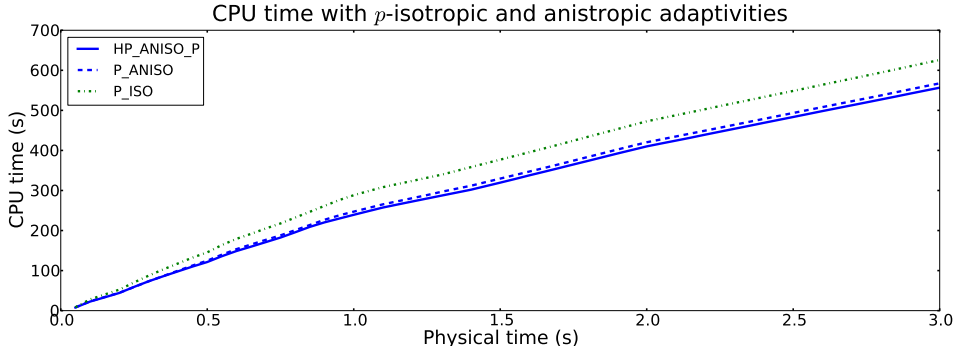


Figure 19: Cumulative CPU times as a function of physical time for multi-mesh configurations with P_ISO, P_ANISO, and HP_ANISO_P adaptivity modes.

HP_ANISO adaptivity mode is the most suitable for the PNP problem due to the small size and relative fastness compared to the other adaptivity modes. A way to optimize the computing time of HP_ANISO will be considered next.

5.4 Time step control of HP_ANISO adaptivity

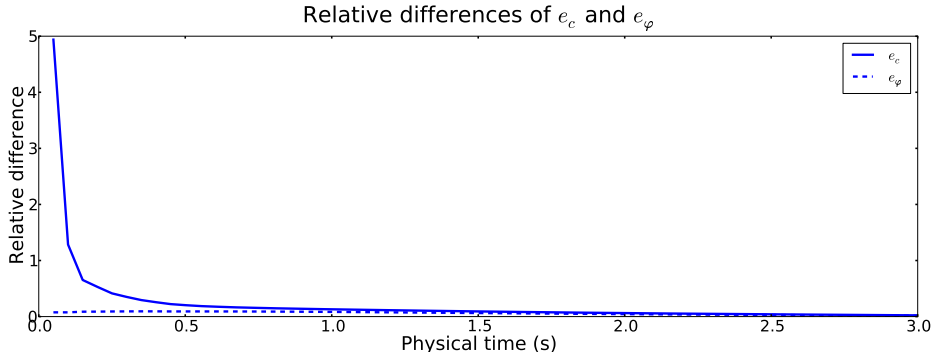


Figure 20: Relative difference e_c^n and e_φ^n .

To optimize the calculation time of HP_ANISO, an adaptive time step control was employed. The classical PID controller was used [3, 15]. Since c and φ change differently in time as was demonstrated in Figs. 7 and 8, the relative changes between the solutions at different time steps were monitored:

$$e_c^n = \frac{\|c^n - c^{n-1}\|}{\|c^n\|}, \quad (5.1)$$

$$e_\varphi^n = \frac{\|\varphi^n - \varphi^{n-1}\|}{\|\varphi^n\|}. \quad (5.2)$$

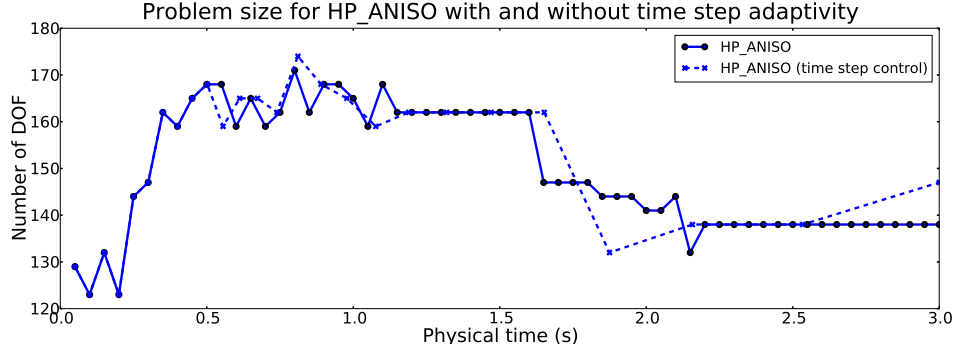


Figure 21: Number of DOF as a function of physical time for HP_ANISO with and without time step adaptivity. The markers on the graphs indicate the time steps.

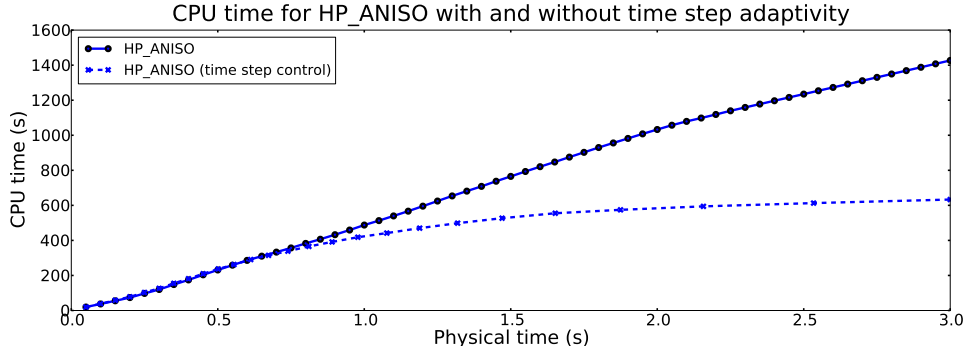


Figure 22: Cumulative CPU times as a function of physical time for HP_ANISO with and without time step adaptivity. The markers on the graphs indicate the time steps.

The relative changes to control the time step was calculated as follows:

$$e^n = \max \{ e_c^n, e_\varphi^n \}. \quad (5.3)$$

If $e^n < \delta$ where $\delta > 0$ is a defined tolerance, then the time step for the next iteration is increased smoothly to

$$\delta \tau^{n+1} = \left(\frac{e^{n-1}}{e^n} \right)^{k_p} \left(\frac{\delta}{e^n} \right)^{k_l} \left[\frac{(e^{n-1})^2}{e^n e^{n-2}} \right]^{k_D} \delta \tau^n, \quad (5.4)$$

where parameters are from [15]:

$$k_p = 0.075, \quad k_l = 0.175, \quad k_D = 0.01. \quad (5.5)$$

The tolerance δ was set to $\delta = 0.25$ in the current optimization example. At this point, the implementation does not support reducing the time step when $e^n \geq \delta$. The calculated e_c^n and e_φ^n are shown in Fig. 20. The HP_ANISO problem size and computing time with

and without time step control are shown in Figs. 21 and 22. The reader can notice that the computing time was reduced more than two times when the time step control was employed.

5.5 HP_ANISO adaptivity with physically more realistic boundary conditions

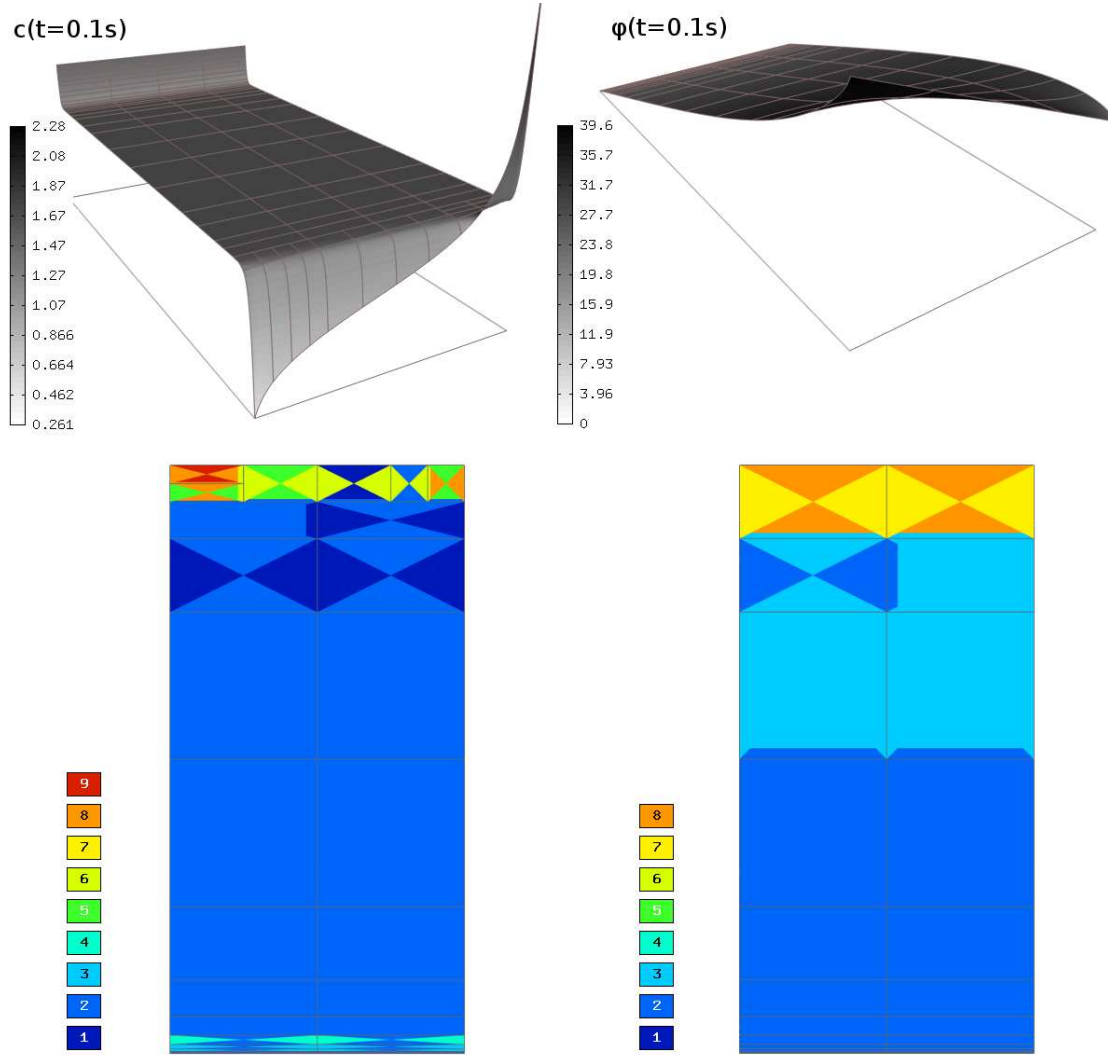


Figure 23: Solutions c and φ and corresponding polynomial degrees of the elements at $t = 0.1$ s. HP_ANISO refinement mode was used. The height in the solution graphs indicates the value.

In real physics calculations, the applied voltage on boundary $\partial\Omega_1$ is not constant. This can be, for instance, due to the high resistance of the electrodes as explained in [6]. To see how the HP_ANISO adaptivity works for such situations, the voltage on the boundary

was applied as follows:

$$\phi_{\Omega_1}(x) = 0.5[V] \frac{x[m]}{\text{width}_{\Omega_1}[m]} + 0.5[V], \quad (5.6)$$

where width_{Ω_1} is the width of the boundary. The given boundary is effectively a linear increase of the voltage from $\phi_{\Omega_1}(x=0) = 0.5 \text{ V}$ to $\phi_{\Omega_1}(x=\text{width}_{\Omega_1}) = 1.0 \text{ V}$. Now the concentration gradient ∇c and the voltage gradient $\nabla \varphi$ are no longer effectively in 1D.

The calculated scaled values c and φ in Ω and corresponding meshes and polynomial degrees of the elements at $t=0.1 \text{ s}$ are shown in Fig. 23. Notice that the solution is different to the one in Fig. 7. The HP_ANISO adaptivity algorithm has particularly increased the polynomial degree and refined the mesh near Ω_1 where a sharp concentration peak exists (compare to Fig. 13). At $t = 3.0 \text{ s}$, the shape of the solutions c and φ are similar to the one in Fig. 8 and therefore the polynomial space and mesh gets adapted accordingly. This example clearly illustrates how the solution of PNP with non-uniform boundary conditions is very dynamic in time and how the HP_ANISO time dependent adaptivity finds an optimal mesh and polynomial space to adapt to the dynamics of the problem.

5.6 Length scale study

The Debye length λ_D is the screening length in the electrolyte solutions. Its numerical value shows the thickness of the layer in the vicinity of the boundaries $\partial\Omega_1$ and $\partial\Omega_2$ where $c \neq 1$. In all the previous simulations, the Debye screening length was determined by the constants in Table 1 and Eq. 3.6: $\lambda_D = XXX$. It is known that computation gets increasingly difficult when reducing the value of λ_D . It was our interest to see how small screening lengths can Hermes HP_ANISO automatic adaptivity handle. The parameter ε was varied as follows:

$$\varepsilon_n = \varepsilon \times 0.5^n,$$

where ε is taken from Table 1. The simulations were run for each ε_n and corresponding λ_D value and maximum number of degrees of freedom and cumulative CPU time were recorded. The simulation time t for each λ_D was chosen to be τ — the characteristic time scale — and each simulation was divided equally into fifteen time steps. No PID controller was used. Fig. XXX shows the maximum number of degrees of freedom during calculation as a function of the Debye length and Fig. XXX shows cumulative CPU time as a function of the Debye length. The simulations up to XXX m screening length were carried out on the initial coarse mesh. However, from $\lambda_D > XXX$ the finer initial mesh had to be used so the existence of the large gradients of the physical fields c and φ near the boundaries could be captured in the first place. The fine mesh allowed simulations with the Debye length down to XXX m. The calculated c and φ at $t=\tau$ for $\lambda_D = XXX$ are shown in Fig. XXX. It appears that when using even finer initial mesh and higher initial polynomial degrees, even smaller Debye lengths could be used when necessary.

6 Conclusion and Outlook

In this work the system of Nernst-Planck-Poisson equations was solved using *hp*-finite element method with adaptive multi-mesh configuration. The weak form, residuals and the Jacobian matrix of the system were explicitly derived and implemented in Hermes *hp*-FEM time dependent adaptive solver. The solution for Nernst-Planck-Poisson problem with two field variables C and ϕ results in very different field gradients in the space and time. When using a conventional low order FEM, finding an optimal mesh for this type of problem such that both the error of the solution and problem size remain small throughout the time dependent solving process is difficult.

In the current work we showed that using the time dependent adaptivity, multi-mesh configuration, and anisotropic *hp* refinements, the problem size remains very small throughout the solving process while maintaining a pre-set relative error of the solution. Namely, Hermes refinement mode HP_ANISO resulted in the smallest and fastest problem solution. Furthermore, using the multi-mesh configuration for the physical fields c and φ — scaled variables for C and ϕ , respectively — was justified. The adaptivity algorithm refined the meshes of φ and c and increased the polynomial degrees of the corresponding spaces differently. The mesh was significantly refined for c and also the maximum polynomial degree was varied in the range of 2...9 whereas for φ , the maximum polynomial degree remained lower. So it is efficient to use multi-mesh in terms of the number of degrees of freedom.

Conclusively, by using *hp*-FEM with adaptive multi-mesh configuration we can possibly reduce the problem size of the Nernst-Planck-Poisson equation system significantly while still maintaining prescribed precision of the solution. We believe, and this is yet to be demonstrated, that this is especially important when dealing with 3D problems in a large physical domain with non-uniform boundary conditions.

Acknowledgments

The second author was partially supported by the Grant Agency of the Academy of Sciences of the Czech Republic under Grant No. IAA100760702, and by the U.S. Department of Energy Research Subcontract No. 00089911. The third author acknowledges the financial support of the U.S. Office of Naval Research under Award N000140910218. The fourth author acknowledges the financial support of the Estonian Ministry of Education, grant #SF0180008s08.

References

- [1] S. Basu and M.M. Sharma, *An improved space-charge model for flow through charged microporous membranes*, Journal of Membrane Science **124** (1997), no. 1, 77–91.
- [2] M.Z. Bazant, K. Thornton, and A. Ajdari, *Diffuse-charge dynamics in electrochemical systems*, Physical Review E **70** (2004), no. 2, 21506.
- [3] L. Dubcova, P. Solin, J. Cerveny, and P. Kus, *Space and Time Adaptive Two-Mesh hp-Finite Element Method for Transient Microwave Heating Problems*, Electromagnetics **30** (2010), no. 1, 23–40.
- [4] S. Nemat-Nasser, *Micromechanics of actuation of ionic polymer-metal composites*, Journal of Applied Physics **92** (2002), no. 5, 2899–2915.
- [5] K.M. Newbury and D.J. Leo, *Linear electromechanical model of ionic polymer transducers-Part I: Model Development*, Journal of Intelligent Material Systems and Structures **14** (2003), no. 6, 333.
- [6] D. Pugal, A. Aabloo, and K. J. Kim, *Dynamic surface resistance model of ipmc*, 2009, pp. 72891E.
- [7] D. Pugal, K. Jung, A. Aabloo, and K.J. Kim, *Ionic polymer-metal composite mechanoelectrical transduction: review and perspectives*, Polymer international **59** (2010), no. 3, 279–289.
- [8] D. Pugal, K. J. Kim, and A. Aabloo, *Modeling the transduction of ipmc in 3d configurations*, 2010, pp. 76441T.
- [9] D. Pugal, K. J. Kim, A. Punning, H. Kasemagi, M. Kruusmaa, and A. Aabloo, *A self-oscillating ionic polymer-metal composite bending actuator*, Journal of Applied Physics **103** (2008), no. 8, 084908.
- [10] M. Shahinpoor and K. J. Kim, *Ionic polymer-metal composites: I. fundamentals*, Smart Materials and Structures **10** (2001), no. 4, 819.
- [11] P. Solin, D. Andrs, J. Cerveny, and M. Simko, *PDE-independent adaptive hp-FEM based on hierarchic extension of finite element spaces*, Journal of computational and applied mathematics **233** (2010), no. 12, 3086–3094.
- [12] P. Solin, J. Cerveny, L. Dubcova, and D. Andrs, *Monolithic discretization of linear thermoelasticity problems via adaptive multimesh hp-FEM*, Journal of computational and applied mathematics **234** (2010), no. 7, 2350–2357.
- [13] P. Solin, L. Dubcova, and I. Dolezel, *Adaptive hp-FEM with arbitrary-level hanging nodes for Maxwells equations*, Advances in Applied Mathematics and Mechanics **2** (2010), no. 4, 518–532.
- [14] P. Solin, L. Dubcova, and J. Kruis, *Adaptive hp-FEM with dynamical meshes for transient heat and moisture transfer problems*, Journal of computational and applied mathematics **233** (2010), no. 12, 3103–3112.
- [15] A. M. P. Valli, G. F. Carey, and A. Coutinho, *Control strategies for timestep selection in simulation of coupled viscous flow and heat transfer*, Communications in Numerical Methods in Engineering **18** (2002), no. 2, 131–139.
- [16] T. Wallmersperger, D. J. Leo, and C. S. Kothera, *Transport modeling in ionomeric polymer transducers and its relationship to electromechanical coupling*, Journal of Applied Physics **101** (2007), no. 2, 024912.